A Comprehensive Benchmarking of the Available Spectral Indices Based on Sentinel-2 for Large-Scale Mapping of Plastic-Covered Greenhouses

Gizem Senel [ID], Manuel A. Aguilar [ID], Fernando J. Aguilar [ID], Abderrahim Nemmaoui [ID], and Cigdem Goksel [ID]

Abstract—**Plastic-covered greenhouses (PCG) have been extensively used in agricultural practices around the world. Remote sensing based on spectral indices is a key asset to monitor the spatial distribution of these structures on a large scale. The primary objective of this research was to conduct a comprehensive benchmarking of the available spectral indices based on Sentinel-2 data for large-scale PCG mapping. For that, eight PCG indices were thoroughly analyzed by systematically investigating their optimal thresholds in five study sites located in Almería (Spain), Antalya (Turkey), Agadir (Morocco), Weifang (China), and Nantong (China), including also different growing seasons. The experimental results demonstrated that the Plastic GreenHouse Index (PGHI) achieved the best PCG mapping accuracy in almost all study sites and growing seasons tested. From the visual analysis carried out on the PGHI mapping results, it was made out that the main misclassification between PCG and background classes took place in water bodies and industrial building land covers, particularly in the Weifang and Nantong study areas. Based on this fact, the original version of PGHI was modified by adding two processes aimed at masking water bodies and industrial buildings. This new composite index, called Improved PGHI (IPGHI), attained better accuracy results in all study sites, especially in Chinese PCG areas. The average F1 score calculated for all the study cases improved from 86.05% using PGHI to 90.51% applying IPGHI. The new approach provided a significant and robust improvement in PCG large-scale mapping for several types of PCG sites, even considering different growing seasons.**

Index Terms—**Greenhouse mapping, large-scale mapping, plastic-covered greenhouses (PCG), Sentinel-2 (S2), spectral indices.**

I. INTRODUCTION

THE first use of a plastic film in agriculture dated in 1948 [1] marked a new era in the practice of intensive agriculture.

Over the last 70 years, the use of plastic-covered greenhouses (PCG) has reached a crucial impact, increasing the yield of horticultural crops and bringing forward the first harvest [2]. In that way, although the area dedicated to PCG has been increasing steadily around the world, published data on it are highly variable. Briassoulis et al. [3] reported that the total area in the major greenhouse production countries worldwide was 30 190 km^2, whereas two recent studies coincided in indicating a global PCG area of around 5000 km^2 [4], [5]. These large differences could be due to how the low tunnels and row covers or mulching were considered in the official data of each country. Moreover, in many countries, there is no separation between greenhouse and field production data.

While plastic can be beneficial to agriculture, its widespread use also raises concerns about its impact on public health by means of the accumulation of microplastics in the environment [6], mainly in soils [7]. A recent report by the Food and Agriculture Organization [7] makes a loud call to coordinate good management practices and curb the disastrous use of plastics throughout the agricultural sector. A recent work published by Liu and Xin [8] reported that the agricultural area of plastic greenhouses in China grew by 42.4% during 2000–2020, mainly in the North China Plain. This fact increased inputs (e.g., nitrogen fertilizer) and area expansion (e.g., building materials), leading to an increase in greenhouse gas emissions. In addition, the presence of PCG affects the esthetic appearance of landscapes. In this vein, remote sensing can provide accurate and regular information to monitor and map spatiotemporal PCG changes around the world.

Remote sensing has been widely applied for mapping PCG and plastic-mulched areas. According to Jiménez-Lao et al. [9], 107 papers were published on this topic throughout the period 2000–2019 based on the Scopus database. Most of these publications used freely accessible medium-resolution optical data from both Landsat 5/7/8 [10], [11], [12], [13], [14], [15], [16], [17] and Sentinel-2 (S2) [18], [19], [20], [21], [22], [23]. In addition, very high resolution (VHR) commercial satellites such as IKONOS, QuickBird, GeoEye-1, or WorldView-2 have been successfully used for mapping PCG [24], [25], [26], [27], [28]. These works applied a wide range of approaches (mainly pixel-based and object-based) and classifiers (maximum likelihood, threshold model, support vector machine, decision tree, and random forest).

In recent years, other high-resolution (HR) and VHR optical imaging spaceborne sensors, such as GaoFen-1, GaoFen-2, Pléiades, WorldView-3, PlanetScope, RapidEye, and SPOT-7, have been used to map PCG by applying the methodologies mentioned above [29], [30], [31], [32], [33], [34]. Moreover, deep learning techniques based on convolutional neural networks have been applied to classify PCG and mulching films using VHR imagery, usually downloaded from open-access sites [35], [36], [37], [38], [39].

The main problem of working on high-spatial-resolution images, usually hard to come by and expensive, lies in the fact that the study areas are usually small, so the proposed methodology cannot be extended to a large scale. Furthermore, object-based approaches (OBIA) using classical machine learning methods are also difficult to be applied to large-scale mapping due to the demand for a large number of samples and computationally intensive models [40].

Two interesting papers focused on testing spectral indices for PCG mapping using S2 images were published in 2022. One of them applied a pixel-based approach on single images [41], whereas the other used S2 time series and OBIA [42]. Both methodologies were tested in a large number of study sites. In this sense, Anamur (Turkey), Almería (Spain), and Nantong and Weifang (China) were considered by Zhang et al. [41], whereas Aguilar et al. [42] worked on Antalya (Turkey), Almería (Spain), Agadir (Morocco), and Bari (Italy). Both works tested several already published PCG spectral indices. These indices included the following.

1) The Greenhouse Vegetable Land Extraction (Vi), proposed by Zhao et al. [43].
2) The Plastic-Mulched Land Cover Index (PMLI), developed by Lu et al. [10].
3) The Moment Distance Index (MDI), originally proposed by Salas and Henebry [44] and later used by Aguilar et al. [13] for mapping PCG.
4) The Plastic Greenhouse Index (PGI), proposed by Yang et al. [16].
5) The Retrogressive Plastic Greenhouse Index (RPGI), also developed by Yang et al. [16].
6) The Greenhouse Detection Index (GDI), introduced in González-Yebra et al. [17].

In addition to the aforementioned indices, it is important to highlight that Zhang et al. [41] developed a new index called the Advanced Plastic Greenhouse Index (APGI). According to the results reported in this work, APGI presented the best experimental results regarding the improvement of PCG information and the suppression of non-PCG background compared with the existing indices. Furthermore, Aguilar et al. [42] also included in their comparison study the Plastic GreenHouse Index (PGHI), proposed by Ji et al. [45] to map PCG from Landsat 8 images using an OBIA approach in the city of Xuzhou (Jiangsu Province, China). It is worth noting that PGHI was the best ranked among all the indices tested by Aguilar et al. [42].

These indices can be used to transfer reliable label information from S2 images to HR images in a pixel–scene–pixel–object transferring process. After that, the transferred HR samples can be used to train the deep semantic segmentation model and
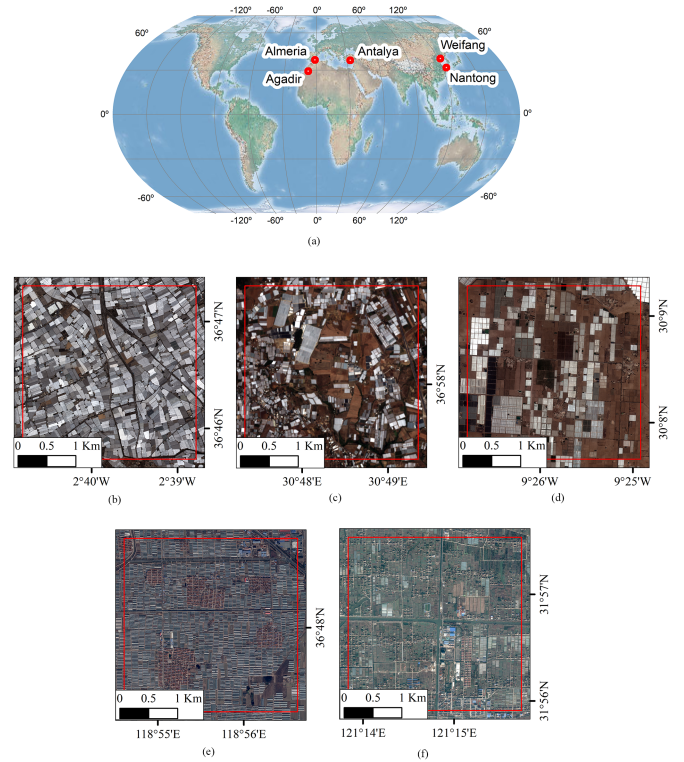

Fig. 1. (a) Global location of the study sites. Detailed view of each of the study areas located in (b) Almería, (c) Antalya, (d) Agadir, (e) Weifang, and (f) Nantong. Red squares depict the study areas covering 3 km by 3 km.

produce PCG mapping results as has already been done by Zhang et al. [46] using APGI.

Taking these last two recently published papers as a starting point, the aim of this article is to highlight the most robust spectral index extracted from S2 for large-scale PCG mapping at present. For that, a fair benchmarking between published spectral indices is mandatory. Consequently, a high number of representative PCG study sites located in different countries, and even considering different growing seasons, should be taken.

II. STUDY AREAS AND DATASETS

A. Study Areas

Five study areas covering 3 km by 3 km and with a large presence of PCG, such as Almería (Spain), Antalya (Turkey), Agadir (Morocco), Weifang (China), and Nantong (China), were selected as study sites in this research (see Fig. 1).

The study site in Almería, located in southeastern Spain, has a very dense PCG concentration [see Fig. 1(b)]. It is centered on the geographic coordinates (WGS84) 36.7764°N and 2.6628°W, being tomato, pepper, cucumber, aubergine, melon, and watermelon the most representative intensive crops [33]. It is essential to keep in mind that the spectral signature of PCG varies over time as a result of the phenological evolution of the crops grown inside them [18], as well as the frequent whitewashing of the roofs to reduce excessive radiation and lower the greenhouse temperature [11].

The study site selected in Antalya is located in the Mediterranean region of Turkey (36.9676°N and 38.8055°E) [see Fig. 1(c)], where mostly vegetables, cut flowers, ornamental plants, and saplings are cultivated. Although there are a few glass greenhouses, plastic is the most typical covering material for the greenhouse structures. Small-size PCG appear mostly in the area, although there are a few large-size ones as well. The density of greenhouses in this area is much lower than in Almeria.

The study site in Souss-Massa plain, Agadir (Morocco), is located at the geographic coordinates 30.1411°N and 9.4323°W [see Fig. 1(d)]. In this case, the agricultural greenhouses PCG are dedicated mainly to tomato cultivation. In addition to large-size PCG, the region includes bare earth, agricultural fields with orchards and outdoor crops [42].

The study area in Weifang (China) [see Fig. 1(e)] is centered on the geographic coordinates 36.8009°N and 118.9265°E. This area is characterized by a continental monsoon climate, which makes the region favorable for crop production. Transparent and translucent plastics are frequently used as covering material for greenhouses [47]. The PCG are densely distributed in Weifang, whereas the size of the individual greenhouse is small and elongated (around 12 m by 60 m), being mostly separated from each other by narrow corridors. The region covers settlement areas, industrial buildings (including blue and concrete roof buildings), and highways surrounded by vegetation.

The last study site in Nantong (China) is located in the northern bank of the Yangtze River [see Fig. 1(f)]. This study area is centered on the geographic coordinates 31.9457°N and 121.2463°E, being the PCG sparsely distributed and appearing in small patches. Moreover, the dense river networks, fragmented farmlands, and widely distributed human settlements create a very complicated landscape that poses a great challenge for PCG mapping [41].

B. Datasets and Preprocessing

Seven cloud-free S2 satellite images corresponding to Almería, Antalya, Agadir, Weifang, and Nantong study sites were used in this work. Additionally, HR images were exclusively used to extract the corresponding ground truth data. The detailed information of the satellite images used in the research is depicted in Table I.

The S2 mission is constituted of two identical satellites, namely Sentinel-2A (S2A) and Sentinel-2B (S2B), both with the multispectral instrument (MSI) sensor. MSI sensors acquire images with 13 spectral bands from visible to shortwave infrared region of the electromagnetic spectrum, with ground sample distance (GSD) ranging from 10 to 60 m. The reader may refer to the S2 User Handbook for more detailed information on the technical specifications of the S2 [48].

Level-2A (L2A) orthorectified products, providing bottom-of-atmosphere reflectance values, were used in this work. Since the spatial resolution of S2 images varies from 10 to 60 m, the spatial resolution of those spectral bands with GSD greater than 10 m was down-sampled to 10 m by applying spatial resampling without interpolation. It should be noted that the

TABLE I
SPECIFICATIONS OF THE SATELLITE IMAGES USED

Study Site	S2	HR		
	Date of Acquisition (Sensor)	Sensor	GSD	Date of Acquisition
Almería	December 26, 2020 (S2A)	WorldView-3	0.3 m	December 25, 2020
Almería	June 14, 2020 (S2B)	WorldView-3	0.3 m	June 11, 2020
Antalya	February 1, 2019 (S2B)	SPOT-7	1.5 m	February 5, 2019
Antalya	July 6, 2019 (S2A)	SPOT-7	1.5 m	July 4, 2019
Agadir	July 7, 2020 (S2B)	Deimos-2	1 m	July 9, 2020
Weifang	December 17, 2021 (S2A)	Pléiades	0.5 m	December 18, 2021
Nantong	December 10, 2019 (S2B)	Pléiades	0.5 m	December 4, 2019

spectral signature of PCG changes considerably between the winter and summer seasons because of the whitewashing of greenhouse roofs and black net coverings, which is very frequent in summer at the study sites of Almería and Antalya. Thus, the S2 images of Almería and Antalya were chosen based on trying to cover these two different seasons. The S2 images of Weifang and Nantong were acquired in December following the recommendations reported by Zhang et al. [41] regarding the favorable climatic conditions and the suitable phenological stages of the crops under the PCG in these regions. It is worth mentioning that the selection of the S2 images was mainly based on the criteria of dates as close as possible to the HR images corresponding to each study area and the absence of clouds (see Table I).

HR orthoimages from WorldView-3, SPOT-7, Deimos-2, and Pléiades were used to attain an accurate ground truth, i.e., individual greenhouses in this case. It should be noted that atmospherically corrected and pan-sharpened HR images for all the study sites were used to ensure an accurate ground truth. The spatial resolution of atmospherically corrected and pan-sharpened HR orthoimages is given in Table I.

All S2 images covering the five study areas were coregistered with their corresponding HR orthoimages by utilizing the AROSICS library, available through the Python programming language [49]. Then, they were clipped according to the planned study areas of 3 km by 3 km.

III. METHODS

A. Spectral Indices

Eight spectral indices specially devised to deal with mapping PCG or plastic-mulched land covers were tested in this work (see Table II). Six of them (APGI, MDI, GDI, PGI, RPGI, and PMLI) have been recently tested by Zhang et al. [41] and Aguilar et al. [42] on several PCG study areas. These eight indices were computed for all S2 images covering the study areas.

Only the required S2 bands for the calculation of the indices were employed in this research [i.e., coastal blue (B1: 60 m spatial resolution), blue (B2: 10 m), green (B3:10 m), red (B4:

TABLE II
SPECTRAL INDICES TESTED FOR MAPPING PCG

	Formula
APGI [41]	$APGI = 100 \times \rho_{coastal} \times \rho_{red} \times \dfrac{2 \times \rho_{NIR} - \rho_{red} - \rho_{SWIR2}}{\times \rho_{NIR} + \rho_{red} + \rho_{SWIR2}}$
MDI [44]	$MDI = MD_{rp} - MD_{lp}$ where; $MD_{rp} = \sum_{i=\lambda_{rp}}^{\lambda_{lp}} \sqrt{(\rho_i^2 + (\lambda_{rp} - i)^2)},$ $MD_{lp} = \sum_{i=\lambda_{lp}}^{\lambda_{rp}} \sqrt{(\rho_i^2 + (i - \lambda_{lp})^2)}$
GDI [17]	$GDI = \dfrac{MDI}{3} - \left(\dfrac{\rho_{blue} - \left(\frac{\rho_{SWIR1} + \rho_{SWIR2}}{2}\right)}{\rho_{blue} + \left(\frac{\rho_{SWIR1} + \rho_{SWIR2}}{2}\right)} \right)$
PGHI [45]	$PGHI = \dfrac{\rho_{blue}}{\rho_{SWIR2}}$
PGI [16]	$PGI = \begin{cases} 0 & when\ NDVI > 0.73 \\ 100 \times \left(\dfrac{\rho_{blue} - (\rho_{NIR} - \rho_{red})}{1 - \frac{(\rho_{blue} + \rho_{green} + \rho_{NIR})}{3}} \right) \\ 0 & when\ NDBI > 0.005 \end{cases}$ where; $NDVI = \dfrac{\rho_{NIR} - \rho_{red}}{\rho_{NIR} + \rho_{red}}$ $NDBI = \dfrac{\rho_{SWIR1} - \rho_{NIR}}{\rho_{SWIR1} + \rho_{NIR}}$
RPGI [16]	$RPGI = \dfrac{\rho_{blue}}{1 - mean\,(\rho_{blue} + \rho_{green} + \rho_{NIR})}$
PMLI [10]	$PMLI = \dfrac{\rho_{SWIR1} - \rho_{red}}{\rho_{SWIR1} + \rho_{red}}$
Index Vi [43]	$Vi = \left(\dfrac{\rho_{SWIR1} - \rho_{NIR}}{\rho_{SWIR1} + \rho_{NIR}} \right) \times \left(\dfrac{\rho_{NIR} - \rho_{red}}{\rho_{NIR} + \rho_{red}} \right)$

10 m), near-infrared (B8: NIR, 10 m), shortwave infrared-1 (B11: SWIR1, 20 m), and SWIR2 (B12: 20 m)], all of them resampled to 10 m. It should be underlined that MDI was calculated using the blue, green, red, NIR, SWIR1, and SWIR2 bands of S2. Moreover, ρ_i in Table II refers to the reflectance of the band i, whereas λ is the wavelength in micrometer.

B. Extraction of Ground Truth and Obtaining Pure Pixels for PCG and Non-PCG

All PCG included in each 3 km by 3 km study site were manually digitized as vector files using the corresponding pan-sharpened HR satellite orthoimages as an on-screen reference. It is important to note that the agricultural greenhouses located in Antalya were divided in PCG (900 in our study area) and glass greenhouses (128 in the study area) based on a field visit. Finally, the 128 glass greenhouses were considered as non-PCG. Furthermore, two different ground truths were carried out in Almería and Antalya for summer and winter, respectively. For
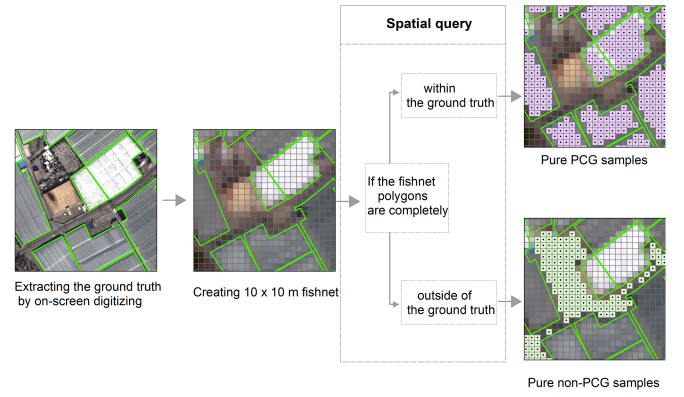

Fig. 2. Methodology to extract pure samples for PCG and non-PCG classes.

all the study sites, the following step consisted of obtaining pure samples (10 m by 10 m pixels in our case), fully representing PCG and non-PCG classes.

For that, a fishnet formed by squared polygons with a side length of 10 m was created. All fishnet polygons that were completely within the digitized PCG were selected via spatial query as pure PCG samples. In the same way, the fishnet polygons that were completely outside of the digitized PCG were selected as pure non-PCG samples. In this way, S2 mixed pixels, which could distort the results of the PCG classification using the eight indices tested in this work, were removed. An illustration of this procedure can be seen in Fig. 2.

C. Thresholds and Classification Accuracy Assessment

The PCG mapping ability of the investigated indices was assessed employing a systematic selection of optimal thresholds similar to that reported by Zhang et al. [41], although using all the pure pixels extracted in the previous section. It is important to note that all those pixels are not a statistical sample, but the total population.

For each PCG index (eight indices) and S2 image (seven cases according to Table I), 50 index thresholds were tested to classify the corresponding image. These thresholds were established by dividing the range of variation of every index over each image (maximum value–minimum value) into 50 intervals. If the pixel value was lower than the specified threshold for GDI, MDI, PMLI, and Vi, or higher for the APGI, PGHI, PGI, and RPGI, then that pixel was identified as PCG. Otherwise, the pixel was labeled as non-PCG. In this way, for each PCG index and case study, 50 binary images labeled as PCG or non-PCG classes were created (i.e., one binary image for each threshold tested).

To evaluate the PCG mapping performance for each index and threshold, a confusion matrix was constructed to compute some accuracy assessment metrics such as user's accuracy or precision (UA), producer's accuracy or recall (PA), overall accuracy (OA), and F1 score (F1). These metrics are calculated by the following equations:

$$UA = \frac{TP}{(TP + FP)} \qquad (1)$$

$$PA = \frac{TP}{(TP + FN)} \tag{2}$$

$$OA = \frac{(TP + TN)}{(TP + TN + FP + FN)} \tag{3}$$

$$F1 = 2 \times \frac{(UA \times PA)}{(UA + PA)}. \tag{4}$$

Here, TP, FP, TN, and FN represent true positive, false positive, true negative, and false negative, respectively. TP denotes the total number of correctly classified PCG pixels, whereas FP represents the total number of pixels misclassified as PCG when they are actually non-PCG pixels. Furthermore, FN represents the PCG pixels incorrectly identified as non-PCG pixels, whereas TN corresponds to the total number of correctly classified non-PCG pixels.

D. Visual Evaluation

Visual evaluation gives an intuitive idea of the capability of the tested indices to highlight PCG pixels and suppress background ones. Note that although mapping accuracies at optimal thresholds were fully investigated at the selected study sites covering a restricted area of 3 km by 3 km, a visual evaluation was conducted for the entirety of each of the S2 images. In this way, we can better assess the performance of each index on land use/land cover types that are more difficult to classify, such as industrial buildings, water canals, water bodies, or open agricultural fields. Industrial buildings and water bodies are often particularly challenging for large-scale PCG mapping [29], [45].

IV. RESULTS

A. PCG Mapping Based on Indices and Optimal Thresholds

To compare the mapping results attained using each PCG index for each study site and season (i.e., for each of the seven S2 images or datasets shown in Table I), the first step was to find out the optimal threshold. This optimal threshold was the threshold, among the 50 tested for each dataset, which produced the best accuracy results in PCG classification based on the F1 score computed using all pure samples. F1 score was used to determine the optimal threshold because this measure takes both UA and PA into account. The total number of pure samples extracted from PCG and non-PCG classes, as well as their percentages for each study case, is presented in Table III. Note that the ground truths in Almería and Antalya for winter and summer were digitalized on HR orthoimages taken at different dates, so it is possible that a few PCG appear or disappear, mainly due to the change of plastic sheet.

Table IV presents the classification accuracy, measured in terms of F1, OA, UA, and PA, for each index and case study from applying the corresponding optimal thresholds. As can be seen in this table, and according to F1 score, PGHI achieved the highest accuracy for all the investigated cases except for Nantong, thus being the best global index tested with a mean value for the F1 score of 86.04%. The ranking of the remaining indices, in terms of the mean values of the F1 score, was MDI (F1

TABLE III
NUMBER OF PURE SAMPLES EXTRACTED FROM PCG AND NON-PCG CLASSES

Study Site	PCG	Non-PCG
Almería Winter	44 952 (78.61%)	12 233 (21.39%)
Almería Summer	44 076 (76.09%)	13 850 (23.91%)
Antalya Winter	17 379 (25.48%)	50 820 (74.52%)
Antalya Summer	16 734 (24.31%)	52 104 (75.69%)
Agadir	23 587 (30.13%)	54 702 (69.87%)
Weifang	6 210 (13.93%)	38 361 (86.07%)
Nantong	4 660 (5.50%)	80 055 (94.50%)

The percentages are represented in parentheses.

= 85.67%), GDI (F1 = 85.60%), RPGI (F1 = 82.96%), APGI (F1 = 78.35%), PMLI (F1 = 75.19%), PGI (F1 = 64.82%), and Vi (F1 = 58.13%). It is important to highlight that the ranking was almost the same for the OA metric: PGHI = 95.44%, GDI = 94.90%, MDI = 93.80%, RPGI = 91.74%, APGI = 90.38%, PMLI = 89.14%, PGI = 81.47%, and Vi = 67.35%. The PGHI, MDI, and GDI indices all returned very similar accuracies, with MDI being the best index in Nantong. Fourth place overall went to RPGI, which presented its worse results in Almería Winter, Agadir, and, especially, in Weifang. In the fifth position was APGI, which showed its best performance in Nantong (second place) and Almería Winter (third position). However, APGI presented very modest accuracies in Antalya (both winter and summer), Agadir, and Weifang. Overall, PMLI, PGI, and Vi achieved lower F1 scores, as already reported by Zhang et al. [41] and Aguilar et al. [42].

In order to have a more detailed view of the differences between the performance of PGHI and APGI (the best indices pointed out by Aguilar et al. [42] and Zhang et al. [41], respectively), we will focus on two of the cases studied: Antalya Summer, where PGHI presented a much better mapping accuracy than APGI, and Nantong, where the exact opposite was true (see Table IV).

Fig. 3 depicts the mapping results of APGI and PGHI using the optimal thresholds corresponding to Antalya Summer study site. It can be made out that the classification mistakes, due to PCG mistakenly classified as non-PCG (FN in orange) and non-PCG erroneously classified as PCG (FP in green), were quite balanced for both indices, being much higher for APGI than for PGHI. Furthermore, most of the glass greenhouses in Antalya Summer were incorrectly classified as PCG when using PGHI. However, the PGHI index allowed us to correctly classify glass greenhouses as non-PCG in Antalya Winter. This finding seems to indicate that the whitewash applied to the greenhouse roofs in summer probably masked any spectral signature patterns typical of glass greenhouses.

Fig. 4 shows the mapping results obtained from applying the APGI and PGHI indices in Nantong. In this study site, the accuracy of PGHI was quite worse than that of APGI. It is clear that the main problem of PGHI is related to the mistakes in green (FP) that affects directly to UA (36.21%). PGHI incorrectly classified as PCG some industrial buildings, a couple of water canals, ponds, and some urban areas. On the

TABLE IV
ACCURACY METRICS FOR THE OPTIMAL THRESHOLDS CORRESPONDING TO THE INDICES INVESTIGATED

Study Cases	Indices	F1 (%)	OA (%)	UA (%)	PA (%)	Thresholds
Almería Winter	APGI	97.43	95.92	96.46	98.42	0.63
	GDI	98.16	97.09	**97.27**	99.07	1.08
	MDI	96.93	95.05	94.71	99.25	3.15
	PGHI	**98.53**	**97.68**	97.97	99.10	1.11
	PGI	95.33	92.80	97.23	93.50	1.19
	PMLI	95.25	92.37	93.29	97.29	0.02
	RPGI	94.23	90.40	89.29	**99.76**	14.05
	Vi	93.67	90.11	94.32	93.02	−0.02
Almería Summer	APGI	92.47	88.02	88.98	96.25	0.66
	GDI	97.17	95.63	96.28	98.07	1.11
	MDI	96.50	94.60	95.61	97.41	2.97
	PGHI	**97.61**	**96.30**	**96.71**	98.52	0.87
	PGI	86.86	76.88	76.82	99.93	−8.47
	PMLI	94.94	92.21	94.27	95.63	0.04
	RPGI	96.13	93.94	94.01	98.34	34.52
	Vi	89.04	81.20	80.34	**99.85**	0.00
Antalya Winter	APGI	76.38	88.63	80.04	73.03	0.50
	GDI	92.01	95.69	86.33	98.49	1.24
	MDI	89.57	94.46	85.14	94.49	3.19
	PGHI	**92.50**	**96.34**	**95.41**	89.76	1.20
	PGI	43.46	58.08	32.90	64.01	1.08
	PMLI	87.25	93.48	85.96	88.57	0.09
	RPGI	90.96	95.15	85.65	96.98	16.74
	Vi	42.15	31.30	26.74	**99.44**	0.01
Antalya Summer	APGI	69.48	86.06	73.30	66.04	1.05
	GDI	89.43	94.67	85.52	93.71	1.19
	MDI	86.49	93.28	83.70	89.47	3.02
	PGHI	**90.51**	**95.38**	**89.33**	**91.72**	0.91
	PGI	41.48	77.19	54.07	33.65	2.72
	PMLI	84.80	92.37	81.37	88.54	0.13
	RPGI	86.06	93.05	83.03	89.31	32.49
	Vi	58.94	72.11	45.60	83.32	0.00
Agadir	APGI	74.11	85.38	79.43	69.45	0.29
	GDI	93.95	96.37	94.39	93.51	1.35
	MDI	86.90	92.39	90.34	83.71	3.14
	PGHI	**95.21**	**97.10**	94.54	**95.90**	0.57
	PGI	56.18	79.43	78.42	43.77	0.23
	PMLI	88.22	92.76	86.54	89.96	0.14
	RPGI	86.58	92.60	**95.39**	79.26	31.24
	Vi	46.42	36.85	31.18	90.80	0.01
Weifang	APGI	63.27	91.13	74.76	54.85	0.30
	GDI	74.81	92.60	71.17	78.84	1.28
	MDI	65.59	89.61	60.90	71.06	3.24
	PGHI	**79.24**	**93.91**	**75.47**	**83.41**	0.77
	PGI	61.41	88.80	59.03	63.98	1.15
	PMLI	46.20	81.48	38.81	57.05	0.15
	RPGI	52.75	80.20	39.51	79.31	11.57
	Vi	55.77	82.01	42.42	81.40	−0.01
Nantong	APGI	75.30	**97.51**	**82.99**	68.91	0.35
	GDI	53.67	92.27	40.04	81.37	1.30
	MDI	**77.69**	97.23	69.78	**87.64**	3.24
	PGHI	48.70	91.38	36.21	74.36	0.72
	PGI	69.00	97.11	84.32	58.39	2.23
	PMLI	29.68	79.28	18.25	79.48	0.23
	RPGI	74.03	96.82	67.18	82.45	15.45
	Vi	20.90	77.90	13.01	53.09	−0.06

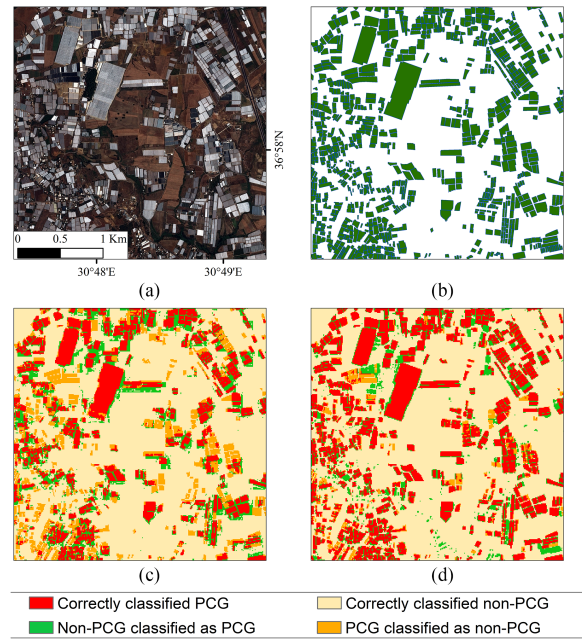Note that the highest values of F1, OA, UA, and PA are in bold for each study site.

Fig. 3. Mapping results using the optimal thresholds of APGI and PGHI in Antalya Summer: (a) RGB VHR orthoimage, (b) ground truth in vector format (PCG are represented by green polygons), (c) APGI classification, and (d) PGHI classification.
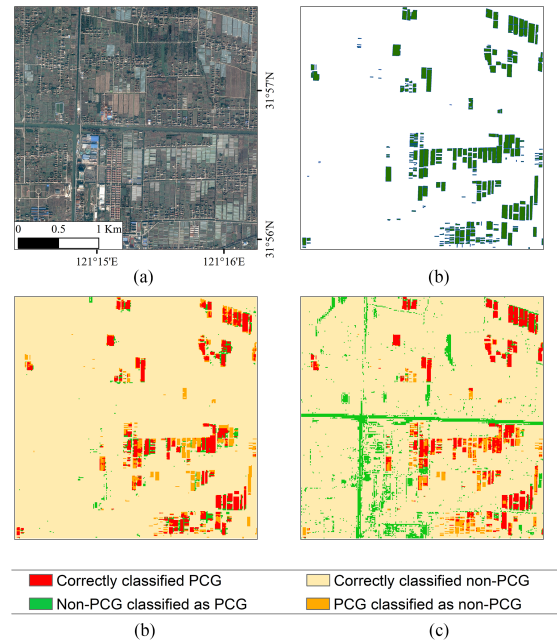

Fig. 4. Mapping results using the optimal thresholds of APGI and PGHI in Nantong: (a) RGB VHR orthoimage, (b) ground truth in vector format (PCG are represented by green polygons), (c) APGI classification, and (d) PGHI classification.

contrary, this index presented a better performance in terms of FN (actual PCG classified as non-PCG; depicted in orange), reaching a PA of 74.36%. On the other hand, in the case of APGI, the mistakes were mainly orange pixels (PA = 68.91%) instead of green pixels (UA = 82.99%). APGI demonstrated its
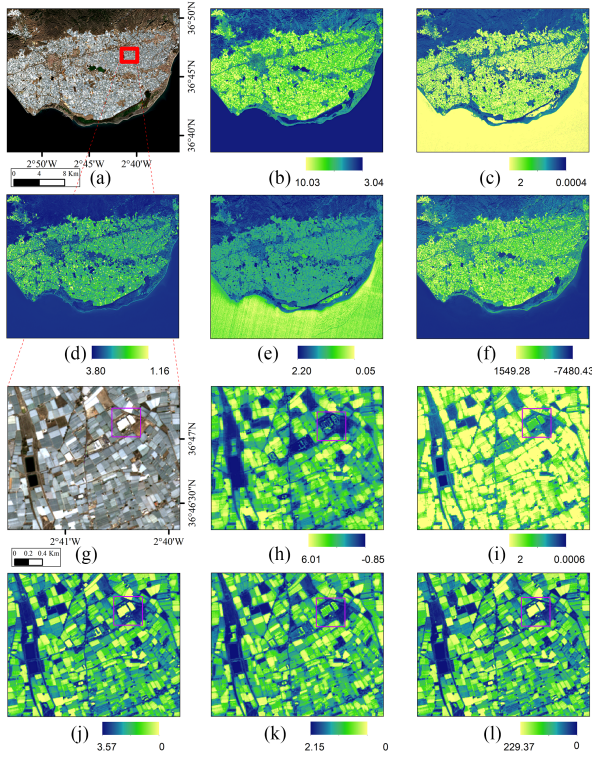
Fig. 5. Visual representation of the indices in the study site Almería Winter: (a) whole orthoimage; (b) APGI; (c) PGHI; (d) MDI; (e) GDI; (f) RPGI; (g) detailed orthoimage; (h) APGI; (i) PGHI; (j) MDI; (k) GDI; (l) RPGI.
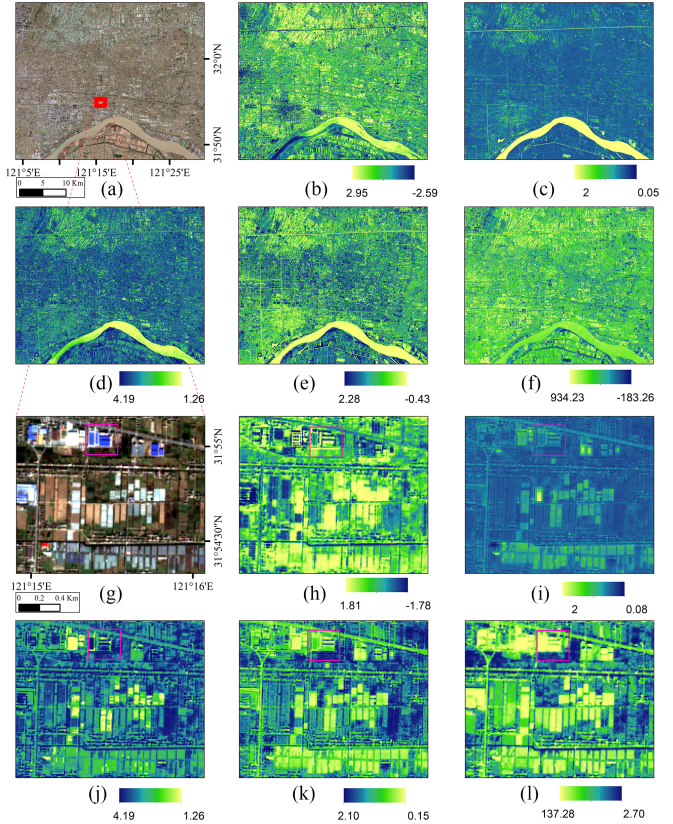

Fig. 6. Visual representation of the indices in the study site Nantong: (a) whole orthoimage; (b) APGI; (c) PGHI; (d) MDI; (e) GDI; (f) RPGI; (g) detailed orthoimage; (h) APGI; (i) PGHI; (j) MDI; (k) GDI; (l) RPGI.

ability to correctly classify troublesome classes, such as water or industrial buildings, although it committed many errors mapping PCG, thus presenting a low PCG recall metric.

B. Visual Evaluation of the Spectral Indices

Figs. 5–7 show the visual evaluation results of APGI, PGHI, MDI, GDI, and RPGI indices computed in some study sites, referring both only to the 3 km by 3 km study areas and to the area more extensive around them. All indices were visualized by equalizing the histogram, using brighter colors (yellow) to represent PCG and darker colors (blue) to refer to non-PCG.

In Fig. 5(b)–(f), it can be seen that APGI, MDI, and RPGI were able to suppress the water class, whereas PGHI and GDI were not. In addition, RPGI presented similar values regarding the PCG class in the coastal and residential areas. It was also noted that APGI and, to a lesser extent, PGHI were able to suppress the industrial building within the purple square, whereas MDI, GDI, and RPGI were unable [see Fig. 5(g)–(l)]. Focusing on the two rectangular-shaped irrigation pools on the west side, they were correctly labeled as non-PCG by all indices [see Fig. 5(g)–(l)].

None of the indices tested were able to completely suppress the Yangtze River in Nantong [see Fig. 6(b)–(f)], probably due to the presence of suspended solids in the water. Regarding the industrial buildings in Nantong, MDI and APGI were capable to classify them as non-PCG better than the other indices [see the purple square in Fig. 6(g)–(l)]. In any case, the classification of the many existing industrial buildings and factories in Nantong and Weifang was generally very weak. For instance,

the industrial building in Weifang circled in Fig. 7(g)–(l) was misclassified as PCG by all indices. However, it is worth noting how industrial buildings with red roofs were well classified as non-PCG. In addition, although the highway seen in Fig. 7(g) was correctly suppressed with APGI and RPGI, it was mistakenly classified as PCG by PGHI, MDI, and GDI [see Fig. 7(h)–(l)]. Paying attention to the lake located in the southeast of the area given in Fig. 7(a), it was labeled as PCG when using the GDI and PGHI indices, whereas APGI correctly assigned it to the background (non-PCG) [see Fig. 7(b)–(f)].

C. PGHI Improved

Table IV revealed that PGHI and GDI consistently reached the highest accuracies in all study sites except Nantong. Besides, as shown in Figs. 5–7, the PGHI and GDI presented deficiencies to correctly assign some background land cover types, including industrial buildings and water bodies or canals, particularly in the study area of Nantong. In fact, both indices showed a very similar pattern to map PCG for all the cases studied. Aguilar et al. [42] pointed out PGHI as the best PCG index in 44 S2 single images taken in Almería, Antalya, and Agadir. In addition, PGHI is an extremely simple index, which makes it computationally fast, particularly when compared to GDI.

With the idea in mind of PGI, where a composite index was proposed by Yang et al. [16] including two restrictions based
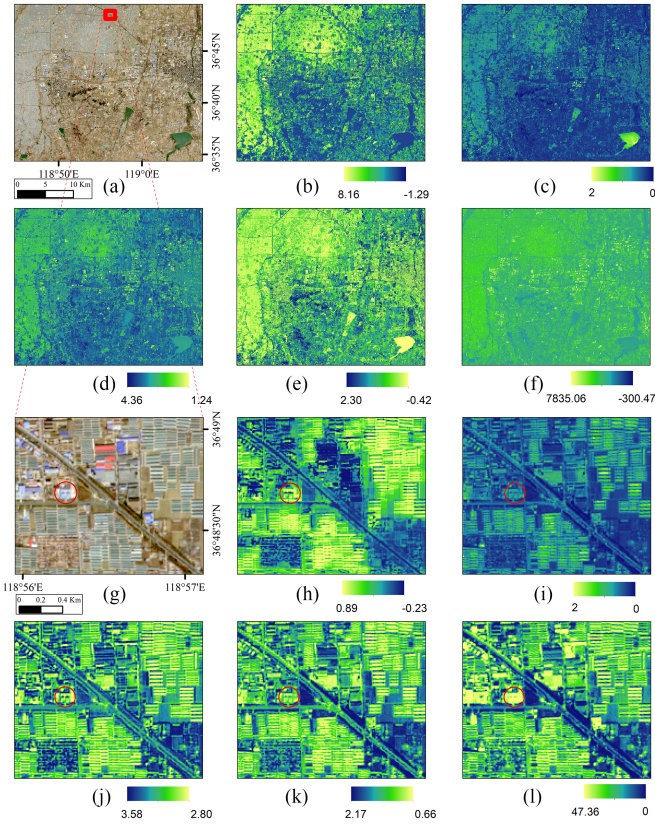
Fig. 7.   Visual representation of the indices in the study site Weifang: (a) whole orthoimage; (b) APGI; (c) PGHI; (d) MDI; (e) GDI; (f) RPGI; (g) detailed orthoimage; (h) APGI; (i) PGHI; (j) MDI; (k) GDI; (l) RPGI.

Fig. 8.   Flowchart of the PGHI improved method (IPGHI).
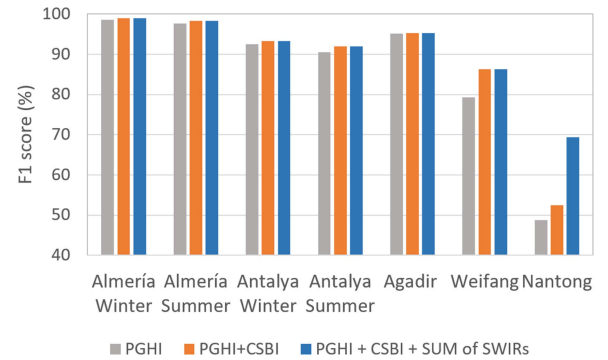
Fig. 9.   F1 scores of IPGHI for each of the three steps.

on NDVI and NDBI, this section proposes an improvement of PGHI to overcome the misclassification of water surfaces and industrial buildings previously highlighted. The new index is called Improved Plastic Greenhouse Index (IPGHI). Starting with the classification corresponding to the best threshold value obtained for PGHI (see Table IV), two more steps were added.

The first step was focused on avoiding the misclassification between PCG and industrial buildings. For that, the color steel buildings index (CSBI) proposed by Ji et al. [45] was applied, mainly created to differentiate buildings with blue roofs and PCG in study sites located in China using Landsat-8 satellite imagery. This index takes advantage of the reflectance difference between the SWIR1 and SWIR2 bands in buildings and PCG land covers

$$\text{CSBI} = \frac{\rho_{\text{SWIR1}}}{\rho_{\text{SWIR2}}}. \quad (5)$$

In our study, CSBI values of 0.800, 0.825, 0.850, 0.875, 0.900, and 0.925 were tested and, for each case studied, the CSBI threshold that achieved the highest F1 score to map PCG and non-PCG was chosen. These values were 0.800 for Almería Winter, Antalya Winter, Antalya Summer, and Weifang, 0.900 for Almería Summer, 0.925 for Agadir, and, finally, 0.850 for Nantong.

The second step included in the calculation of the IPGHI index consisted of masking out water bodies (to be later labeled
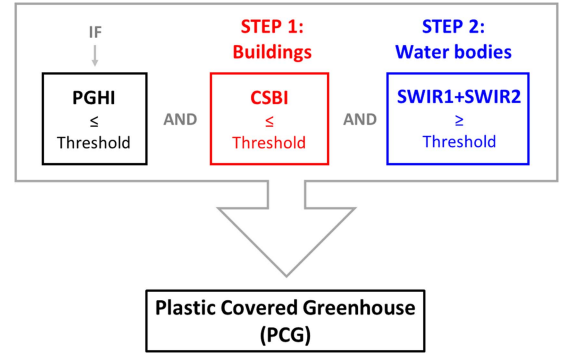
as background) that usually were misclassified as PCG. In this work, the sum of the reflectance values of SWIR1 and SWIR2 was used to distinguish water surfaces as it performed satisfactorily in our study sites. This method is based on the fact that water presents low values of SWIR1 and SWIR2. It is also true that pixels belonging to other classes, such as very dark buildings and even vegetation, might present low values in relation to the sum of the SWIR bands. Nevertheless, it should be noted that the last is not a problem in the particular case of mapping PCG. Finally, threshold values for this index of 0.11 were used in Almería and Antalya (for both Winter and Summer). A value of 0.18 was applied in Weifang, whereas 0.22 was the ideal value in Nantong and Agadir.

Fig. 8 depicts the flowchart to classify PCG by applying the IPGHI index based method considering the two aforementioned steps. For instance, in the case of Nantong study site, the three corresponding thresholds would be 0.72, 0.85, and 0.22 for PGHI, CSBI, and the sum of SWIR bands, respectively.

Since there are no water bodies in the 3 km by 3 km study areas located in Almería, Antalya, and Agadir, the application of the threshold to mask out water did not improve accuracy in these cases (see Fig. 9). On the other hand, the most striking study areas are undoubtedly Weifang and Nantong. In Weifang, an accuracy increment of about 7.1% was achieved when step 1 (CSBI threshold) was added to PGHI. Since there was no presence of water bodies in this study area, no significant increase was observed in terms of F1 score after adding step 2
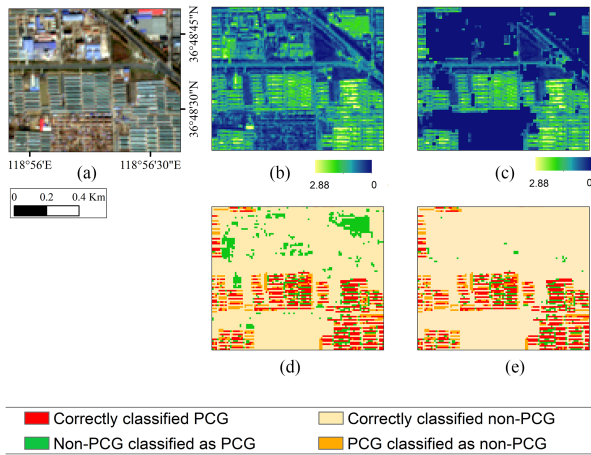
Fig. 10. Detailed area in Weifang: (a) RGB S2 image, (b) PGHI index, (c) IPGHI index, (d) PGHI-based classification map, and (e) IPGHI-based classification map.
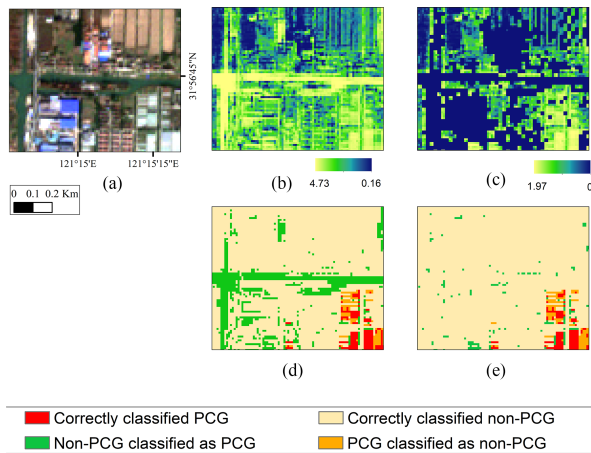

Fig. 11. Detailed area in Nantong: (a) RGB S2 image, (b) PGHI index, (c) IPGHI index, (d) PGHI-based classification map, and (e) IPGHI-based classification map.

(sum of SWIR bands). In the study area of Nantong (3 km by 3 km), an increase of 3.8% was observed when step 1 was added to PGHI, whereas a very significant improvement of 16.9% in accuracy was achieved after applying step 2. The improvement in accuracy after the application of step 1 was mainly because CSBI was able to remove the misclassification between PCG and white or blue roof industrial buildings [42], [45].

Fig. 10 shows a detailed area in Weifang where it can be seen that industrial buildings, which were wrongly classified as PCG using PGHI [green pixels in Fig. 10(d)], were classified as non-PCG when applying IPGHI [see Fig. 10(e)]. Moreover, the detailed area of Nantong represented in Fig. 11 depicts that the misclassification of the water canals given in green color was also avoided when using IPGHI.

The F1 score values for APGI, PGHI, and IPGHI computed from only using pure pixels belonging to the seven datasets of 3 km by 3 km are shown in Table V. Looking at the last row, the average values of F1 score for PGHI had an overall increase of 7.7 percentage points over APGI. IPGHI achieved

TABLE V
PCG MAPPING ACCURACIES OF AGPI-, PGHI-, AND IPGHI-BASED METHODS FOR BOTH PURE PIXELS AND ALL PIXELS

	F1 score (%) Pure pixels and 10 m GSD			F1 score (%) All pixels and 2 m GSD		
	APGI	PGHI	IPGHI	APGI	PGHI	IPGHI
Almería Winter	97.43	98.53	99.00	92.04	93.07	93.35
Almería Summer	92.47	97.61	98.30	88.25	92.65	93.05
Antalya Winter	76.38	92.52	93.28	70.99	84.83	85.29
Antalya Summer	69.48	90.51	92.00	64.22	81.59	82.33
Agadir	74.11	95.21	95.32	71.14	89.38	89.40
Weifang	63.27	79.24	86.32	48.35	64.53	65.21
Nantong	75.30	48.70	69.37	67.27	46.00	63.91
Average value	78.35	86.05	90.51	71.75	78.87	81.79

the best average accuracies in this study, improving by almost 4.47 percentage points the original F1 score of PGHI. Actually, IPGHI improved the results of PGHI mainly in Weifang (correcting the misclassification of industrial buildings through CSBI) and Nantong (correcting the misclassification of both industrial buildings and water bodies).

Finally, a more realistic classification accuracy assessment was carried out following the pixel-based strategy employed by Nemmaoui et al. [19] and Aguilar et al. [42]. In this assessment, each ground truth was converted into raster format with 2 m GSD. Furthermore, classification methods based on APGI, PGHI, and IPGHI were applied on the seven 3 km-sided S2 images used in this work, but now they were resampled to 2 m GSD (without interpolation) including all pixels (i.e., mixed pixels were not removed). The corresponding reference data (ground truth) and classification maps derived from using APGI, PGHI, and IPGHI, both with 2 m GSD, were compared for each study case to attain the confusion matrices.

Table V shows the accuracy results yielded by APGI, PGHI, and IPGH classifications working on 2 m GSD images and all pixels strategy.

V. DISCUSSION

A. PCG Mapping Based on Indices and Optimal Thresholds

Although the main sample areas cover 3 km by 3 km, which contains 300 × 300 pixels working on S2 10 m GSD images, we have to be in mind that seven studied cases located in five study sites were considered in this work. Moreover, all pixels (not only a sample) in these seven cases were included in the accuracy assessment. Thus, the accuracy assessment for pure pixels was based on 459 723 pixels, whereas almost 16 million pixels were studied when the strategy of all pixels and 2 m GSD was carried out (see Table V). The work published by Yang et al. [16] to develop PGI were supported by three accuracy assessment based on 28 224, 1135, and 784 Landsat 30 m GSD pixels, respectively. This work was mainly based on one sample

area of 5 km by 5 km. Furthermore, Zhang et al. [41] used 40 000 pixels from S2 included in five study sites to propose APGI.

The sample areas used in this investigation included different land covers such as PCG (a great variety of sizes and type of plastic), glass greenhouses, residential building, industrial building (red roof, blue roof, and concrete roof), water (canals and agricultural ponds), bare solid, and vegetation. In addition, we carried out a thorough visual evaluation of the PCG indices in S2 images larger than 100 km by 100 km [see, for example, Figs. 5(a), 6(a), and 7(a)] for all the seven cases studied. The last give us important information to evaluate the effectiveness and robustness of each index.

Zhang et al. [41] pointed out APGI as the best global PCG index working on five study sites with an average F1 score of 91.62%. The rest of the indices achieved by Zhang et al. [41] were MDI (F1 = 85.16%), PMLI (F1 = 72.40%), GDI (F1 = 71.73%), PGI (F1 = 71.32%), and Vi (F1 = 46.52%). They also stated that MDI performed quite well in the Mediterranean region, performing poorly in Weifang and Nantong. However, it was quite intriguing that the results achieved for GDI were so poor compared to APGI or MDI (it is important to note that Zhang et al. [41] did not test PGHI). These notable differences are attributed to the presence of the water bodies land cover, which is, most of the time, correctly classified as non-PCG by APGI and MDI, but not using GDI. Note that the study areas used by Zhang et al. [41] were very large, including even large sea masses, whereas in the study sites used in our work (3 km by 3 km) there was hardly any water (only in Nantong there were a couple of water canals).

Very high F1 score values were achieved in Almería (see Table IV), varying from 86.86% (PGI in Almería Summer) to 98.53% (PGHI in Almería Winter). It was mainly due to the extremely high PCG density in this study area. Overall, the attained accuracies were worse in study sites with low percentages of the area covered by PCG (e.g., Weifang and Nantong; see Table III). Indeed, PCG scattered patches are often difficult to discriminate because their spectral signature is confused with the signature of other land covers. Consequently, the accuracy achieved by Zhang et al. [41] for APGI and MDI in Anamur (Turkey), a study area with an impressive concentration of PCG, was almost identical to those reached in Almería. Similarly, classification was challenging in Weifang due to the small size of the greenhouses and the close separation between them of about 9.5 m (less than the 10 m pixel size of S2).

The standard deviation considering the seven optimal threshold values (corresponding to the seven datasets tested) and the best indices were 0.10 for MDI and GDI, 0.22 for PGHI, and 0.27 in the case of AGPI. Note that the lower standard deviation value, the better performance of the index studied. Zhang et al. [41] reported a standard deviation across five datasets of 0.06 for GDI, 0.07 for MDI, and 0.09 for APGI.

The optimal threshold values for PGHI were consistent for Almería and Antalya Winter (1.11 and 1.20, respectively) and Almería and Antalya Summer (0.87 and 0.91, respectively), also being similar in the China study sites (0.77 for Weifang and 0.72 for Nantong). Ji et al. [45] reported threshold values for PGHI ranging from 0.43 to 0.68 in study sites located in China, in this case using Landsat-8 images. On the other hand, Aguilar et al. [42] used an OBIA approach on 14 S2 images taken in 2020, reporting mean cutting values of PGHI of 1.12, 0.52, and 0.71 for Almería, Agadir, and Antalya study sites, respectively.

Overall, GDI and MDI presented thresholds more consistent considering all the study sites. The optimal threshold values published by Zhang et al. [41] ranged between 2.95 and 3.13 for MDI and 1.18 and 1.35 for GDI, whereas in this work they ranged from 2.97 to 3.24 for MDI and from 1.08 to 1.35 for GDI, which turn out to be pretty close values. In the case of APGI, Zhang et al. [41] provided values from 0.25 to 0.43, whereas in the current study the optimal threshold values were ranging from 0.29 (Agadir) to 1.05 (Antalya Summer). Moreover, Zhang et al. [46] recommended APGI thresholds from 0.41 to 0.43 in Mediterranean regions (Spain and Turkey) and 0.25 in China areas (Nantong and Weifang). In our study, quite different optimal thresholds for APGI were set in 0.63, 0.66, 0.50, and 1.05 for the Mediterranean regions (i.e., Almería and Antalya in Winter and Summer) and 0.30 and 0.35 in China study sites (Weifang and Nantong).

The spectral reflectance of PCG depends on several factors. Among others, the whitewashing applied to reduce the temperature inside, the kind of greenhouse (geometry of roof and disposition of roof windows), the crop type under the plastic sheets, and even the relationship between the light incidence angle and the remote sensor point of view [28]. However, and despite this fact, it can be concluded that the obtained optimal thresholds for most of the indices studied in this research are in line with those reported in other investigations, although it was highly dependent on the characteristics of the study area.

B. Visual Evaluation of the Spectral Indices

From the detailed and extended views shown in Figs. 5–7, and focusing on PGHI and APGI indices, we can highlight two facts.

First, PGHI presented serious misclassification problems dealing with water class (sea, canals, ponds, lakes, rivers, etc.). By contrast, Zhang et al. [41] argued that APGI has the ability to label as background (i.e., non-PCG) several land cover types, including water and artificial surfaces. However, it should be noted that APGI was not able to suppress the water in part of the Yangtze River in the case of Nantong study site [see the southern part in Fig. 6(b)]. This was because the spectral reflectance of the water varies along the river, probably due to the presence of suspended solids such as clay or silt.

Second, the classification of existing industrial buildings and factories, particularly in Nantong and Weifang, resulted to be quite poor, mainly using PGHI.

C. PGHI Improved

The inclusion of a step to mask out the water land cover was already carried out by Lu et al. [10] and Ji et al. [45] for mapping plastic-mulched land cover and PCG, respectively. Due to the large differences in spectral signatures that this land cover can present (e.g., dark water bodies, bright water bodies, water bodies with different suspended solids), it is not trivial to find a robust index to work well in all cases. However, the methods based on handcrafted features have already demonstrated fine

performance in optical images [50], [51], [52], being the normalized difference water index the best-known feature. Actually, the way to mask out water bodies could vary depending on the study site. Moreover, we can use the S2 Scene Classification Layer included in L2A products for removing for the class PCG the pixels classified as water.

Concerning the thresholds applied for steps 1 (CBSI) and 2 (sum of the SWIR bands), Ji et al. [45] reported threshold values for CSBI ranging between 0.83 and 0.87 using Landsat 8 imagery in two study sites located in China. However, it is important to note that each PCG study area is different and lighting and atmospheric conditions can vary significantly. Thus, it is very difficult, almost impossible, to find a fixed threshold value that works well for all the cases studied. However, a fairly narrow range of values is given within which the optimal value of CBSI (0.800 to 0.925) and sum of SWIR (0.11 to 0.22) should lie. In fact, it is quite fast to decide which threshold values to choose for a given zone.

Compared to the results shown in Table V for 10 m GSD pure pixels, Zhang et al. [41] achieved an average F1 score for APGI working on five S2 images of 91.62%, also reporting F1 score values of 95.21%, 95.24%, and 96.20% for Almería Summer, Almería Winter, and Anamur, respectively. These values are similar to those attained in this work by applying APGI to the two seasons in the study site of Almería. However, Zhang et al. [41] achieved an impressive F1 score for APGI-based classification in Weifang (80.56%) and Nantong (90.91%), much higher than the values obtained in this work at the same study sites.

Regarding the accuracy results depicted in Table V with all pixels and 2 m GSD, following the same methodology for the accuracy assessment, Aguilar et al. [42] reported F1 score values of 94.28%, 90.88%, and 91.08% in Almería, Agadir, and Antalya, respectively. They used an OBIA approach with S2 time series and statistical features mainly based on PGHI. These figures could be considered close to the best possible values achievable for the considered study site. In this way, the accuracies in Table V were yielded by IPGH-based classification, reaching values very close to those reported by Aguilar et al. [42] in Almería and Agadir, being a little worse in Antalya (see Table V). It is important to note here that the PCG area studied by Aguilar et al. [42] was located in Kumluca (Antalya), presenting a higher concentration of PCG than the study area of Antalya used in the current work.

Comparing the F1 score values attained for the accuracy assessment strategies of 10 m GSD pure pixels and 2 m GSD all pixels in Table V, it is important to underline that the most significant decreases were computed in Weifang for all indices. This was due to the particular shape of most of the PCG in this study area, being very long and narrow (around 12 m), with a separation between them of about 9.5 m [see Fig. 10(a)]. In this sense, medium-resolution S2 images with 10 m GSD were insufficient to deal with this type of PCG, so many misclassifications were found in the mixed pixels containing spectral signatures coming from both PCG and non-PCG. This fact was already noted by Zhang et al. [46] using S2 and especially working on Landsat 8 [16], [41].

Finally, it is important to highlight that 3 km by 3 km study sites perhaps can seem too small to assess the large-scale mapping abilities of the tested indices. To deal with this, the full S2 scenes (100 km × 100 km) were also used in the visual evaluation. Exhaustive further investigations, similar to the published by Liu et al. [53] for urban areas, should be carried out to confirm the results presented in this work about PCG indices.

VI. CONCLUSION

In this article, the PCG mapping ability of eight well-known spectral indices has been comprehensively addressed by considering S2 images of five representative agricultural areas located in Spain, Morocco, China, and Turkey, taking into account even different growing seasons. In order to undertake a fair comparison of the different indices, their optimal thresholds were calculated taking into account all the existing pure pixels (i.e., both PCG and non-PCG pure pixels) in each of the seven cases considered. After that, the accuracy assessment of PCG classification was carried out by means of classical accuracy metrics derived from the corresponding confusion matrices. Finally, the performance of the tested indices was discussed quantitatively and visually.

According to the quantitative evaluation using the 3 km by 3 km sample areas, PGHI stood out among all the tested indices showing the best performance in all the investigated study sites except in Nantong (China). The best F1 score values yielded by PGHI were 98.53%, 97.61%, 92.50%, 90.51%, 95.21%, 79.24%, and 48.70% for Almeria Winter, Almeria Summer, Antalya Winter, Antalya Summer, Agadir, Weifang, and Nantong, respectively. The global ranking of the eight tested indices based on their F1 score mean values for the seven case studies was PGHI (F1 = 86.04%), MDI (F1 = 85.67%), GDI (F1 = 85.60%), RPGI (F1 = 82.99%), APGI (F1 = 78.35%), PMLI (F1 = 75.19%), PGI (F1 = 64.82%), and Vi (F1 = 58.13%). PGHI also showed a robust and stable threshold in all investigated cases, presenting an acceptable standard deviation of 0.27 with a mean value of 0.88. In addition, it should be noted that PGHI is computed extremely easily using only two bands [Blue (B2) and SWIR2 (B12)], giving it a distinct advantage over other indices, especially in large-scale PCG mapping.

Although PGHI achieved the best accuracies (in terms of OA and F1 score) in most of the study areas 3 km-sided, the visual evaluation of more extended areas highlighted misclassification problems in relation with the presence of water bodies and industrial buildings, particularly in Weifang and Nantong study sites. On this basis, a new composite index, called IPGHI, was proposed in this work for masking out water bodies and buildings. As a result, IPGHI based classification method significantly increased PCG's mapping accuracy, specifically in Weifang (F1 score of 86.32%) and Nantong (F1 score of 69.34%). This new pixel-based approach provided a significant and robust improvement in the accuracy of mapping PCG located in different areas of intensive agriculture around the world.

and Pléiades images were provided by the European Space Agency through two Third Party Mission projects with IDs 51010 and PP0087500, respectively. Finally, this study takes part in the general research lines promoted by the Agrifood Campus of International Excellence ceiA3.

REFERENCES

[1] J. C. Garnaud, "Plasticulture magazine: A milestone for a history of progress in plasticulture," *Plasticulture*, vol. 1, no. 119, pp. 30–43, 2000.

[2] E. Espí, A. Salmerón, A. Fontecha, Y. García, and A. I. Real, "Plastic films for agricultural applications," *J. Plast. Film Sheeting*, vol. 22, no. 2, pp. 85–102, Apr. 2006, doi: 10.1177/8756087906064220.

[3] D. Briassoulis, G. Dougka, D. Dimakogianni, and I. Vayas, "Analysis of the collapse of a greenhouse with vaulted roof," *Biosyst. Eng.*, vol. 151, pp. 495–509, Nov. 2016, doi: 10.1016/j.biosystemseng.2016.10.018.

[4] Rabobank Research Food & Agribusiness, "The 2018 world vegetable map," Jan. 2018. [Online]. Available: https://research.rabobank.com/far/en/sectors/regional-food-agri/world_vegetable_map_2018.html

[5] Cuesta Roble Consulting, "World greenhouse vegetable statistics - 2019 updates," 2019. [Online]. Available: https://www.cuestaroble.com/statistics.html

[6] J. R. Jambeck et al., "Plastic waste inputs from land into the ocean," *Mar. Pollut.*, vol. 347, no. 6263, pp. 768–771, Feb. 2015, doi: 10.1126/science.1260352.

[7] Food and Agriculture Organization of the United Nations (FAO), "Assessment of agricultural plastics and their sustainability: A call for action," Rome (Italy): 2021, doi: 10.4060/cb7856en.

[8] X. Liu and L. Xin, "Spatial and temporal evolution and greenhouse gas emissions of China's agricultural plastic greenhouses," *Sci. Total Environ.*, vol. 863, no. 10, Mar. 2023, Art. no. 160810, doi: 10.1016/j.scitotenv.2022.160810.

[9] R. Jiménez-Lao, F. J. Aguilar, A. Nemmaoui, and M. A. Aguilar, "Remote sensing of agricultural greenhouses and plastic-mulched farmland: An analysis of worldwide research," *Remote Sens.*, vol. 12, no. 16, 2020, Art. no. 2649, doi: 10.3390/rs12162649.

[10] L. Lu, L. Di, and Y. Ye, "A decision-tree classifier for extracting transparent plastic-mulched landcover from Landsat-5 TM images," *IEEE J. Sel. Topics Appl. Earth Observ. Remote Sens.*, vol. 7, no. 11, pp. 4548–4558, Nov. 2014.

[11] M. Aguilar, A. Vallario, F. Aguilar, A. Lorca, and C. Parente, "Object-based greenhouse horticultural crop identification from multi-temporal satellite imagery: A case study in Almeria, Spain," *Remote Sens.*, vol. 7, no. 6, pp. 7378–7401, Jun. 2015, doi: 10.3390/rs70607378.

[12] A. Novelli and E. Tarantino, "Combining ad hoc spectral indices based on LANDSAT-8 OLI/TIRS sensor data for the detection of plastic cover vineyard," *Remote Sens. Lett.*, vol. 6, no. 12, pp. 933–941, Sep. 2015, doi: 10.1080/2150704x.2015.1093186.

[13] M. Aguilar, A. Nemmaoui, A. Novelli, F. Aguilar, and A. García Lorca, "Object-based greenhouse mapping using very high resolution satellite data and Landsat 8 time series," *Remote Sens.*, vol. 8, no. 6, Jun. 2016, Art. no. 513, doi: 10.3390/rs8060513.

[14] C. F. Wu, J. S. Deng, J. S. K. Wang, L. G. Ma, and A. R. S. Tahmassebi, "Object-based classification approach for greenhouse mapping using Landsat-8 imagery," *Int. J. Agriculture Biol. Eng.*, vol. 9, no. 1, pp. 79–88, 2016, doi: 10.3965/j.ijabe.20160901.1414.

[15] Hasituya and Z. Chen, "Mapping plastic-mulched farmland with multi-temporal Landsat-8 data," *Remote Sens.*, vol. 9, no. 6, Jun. 2017, Art. no. 557, doi: 10.3390/rs9060557.

[16] D. Yang, J. Chen, Y. Zhou, X. Chen, X. Chen, and X. Cao, "Mapping plastic greenhouse with medium spatial resolution satellite data: Development of a new spectral index," *ISPRS J. Photogramm. Remote Sens.*, vol. 128, pp. 47–60, Jun. 2017, doi: 10.1016/j.isprsjprs.2017.03.002.

[17] O. González-Yebra, M. A. Aguilar, A. Nemmaoui, and F. J. Aguilar, "Methodological proposal to assess plastic greenhouses land cover change from the combination of archival aerial orthoimages and Landsat data," *Biosyst. Eng.*, vol. 175, pp. 36–51, Nov. 2018, doi: 10.1016/j.biosystemseng.2018.08.009.

[18] A. Novelli, M. A. Aguilar, A. Nemmaoui, F. J. Aguilar, and E. Tarantino, "Performance evaluation of object based greenhouse detection from Sentinel-2 MSI and Landsat 8 OLI data: A case study from Almería (Spain)," *Int. J. Appl. Earth Observ. Geoinf.*, vol. 52, pp. 403–411, Oct. 2016, doi: 10.1016/j.jag.2016.07.011.

[19] A. Nemmaoui, M. A. Aguilar, F. J. Aguilar, A. Novelli, and A. García Lorca, "Greenhouse crop identification from multi-temporal multi-sensor satellite imagery using object-based approach: A case study from Almería (Spain)," *Remote Sens.*, vol. 10, no. 11, Nov. 2018, Art. no. 1751, doi: 10.3390/rs10111751.

[20] L. Lu, Y. Tao, and L. Di, "Object-based plastic-mulched landcover extraction using integrated Sentinel-1 and Sentinel-2 data," *Remote Sens.*, vol. 10, no. 11, Nov. 2018, Art. no. 1820, doi: 10.3390/rs10111820.

[21] P. Hao, Z. Chen, H. Tang, D. Li, and H. Li, "New workflow of plastic-mulched farmland mapping using multi-temporal Sentinel-2 data," *Remote Sens.*, vol. 11, no. 11, Jun. 2019, Art. no. 1353, doi: 10.3390/rs11111353.

[22] G. A. Perilla and F. J. Mas, "High-resolution mapping of protected agriculture in Mexico, through remote sensing data cloud geoprocessing," *Eur. J. Remote Sens.*, vol. 52, no. 1, pp. 532–541, Nov. 2019, doi: 10.1080/22797254.2019.1686430.

[23] Y. Xiong, Q. Zhang, X. Chen, A. Bao, J. Zhang, and Y. Wang, "Large scale agricultural plastic mulch detecting and monitoring with multi-source remote sensing data: A case study in Xinjiang, China," *Remote Sens.*, vol. 11, no. 18, Sep. 2019, Art. no. 2088, doi: 10.3390/rs11182088.

[24] F. Agüera, M. A. Aguilar, and F. J. Aguilar, "Detecting greenhouse changes from QuickBird imagery on the Mediterranean coast," *Int. J. Remote Sens.*, vol. 27, no. 21, pp. 4751–4767, Mar. 2006, doi: 10.1080/01431160600702681.

[25] F. Agüera, F. J. Aguilar, and M. A. Aguilar, "Using texture analysis to improve per-pixel classification of very high resolution images for mapping plastic greenhouses," *ISPRS J. Photogramm. Remote Sens.*, vol. 63, no. 6, pp. 635–646, Nov. 2008, doi: 10.1016/j.isprsjprs.2008.03.003.

[26] C. Arcidiacono and S. M. C. Porto, "Improving per-pixel classification of crop-shelter coverage by texture analyses of high-resolution satellite panchromatic images," *J. Agricultural Eng.*, vol. 42, no. 4, pp. 9–16, 2012, doi: 10.4081/jae.2011.4.9.

[27] D. Koc-San, "Evaluation of different classification techniques for the detection of glass and plastic greenhouses from WorldView-2 satellite imagery," *J. Appl. Remote Sens.*, vol. 7, no. 1, 2013, Art. no. 073553, doi: 10.1117/1.Jrs.7.073553.

[28] M. Aguilar, F. Bianconi, F. Aguilar, and I. Fernández, "Object-based greenhouse classification from GeoEye-1 and WorldView-2 stereo imagery," *Remote Sens.*, vol. 6, no. 5, pp. 3554–3582, Apr. 2014, doi: 10.3390/rs6053554.

[29] L. Shi, X. Huang, T. Zhong, and H. Taubenböck, "Mapping plastic greenhouses using spectral metrics derived from GaoFen-2 satellite data," *IEEE J. Sel. Topics Appl. Earth Observ. Remote Sens.*, vol. 13, pp. 49–59, Feb. 2020, doi: 10.1109/JSTARS.2019.2950466.

[30] Z. C. Hasituya, F. Li, and Y. Hu, "Mapping plastic-mulched farmland by coupling optical and synthetic aperture radar remote sensing," *Int. J. Remote Sens.*, vol. 41, no. 20, pp. 7757–7778, 2020, doi: 10.1080/01431161.2020.1763510.

[31] H. Tuya, Z. Chen, Z. Li, and F. Li, "Potential of Pléiades and Radarsat-2 data for mapping plastic-mulched farmland using object-based image analysis," *Can. J. Remote Sens.*, vol. 47, no. 4, pp. 607–620, Jul. 2021, doi: 10.1080/07038992.2021.1946384.

[32] F. Bektas Balcik, G. Senel, and C. Goksel, "Object-based classification of greenhouses using Sentinel-2 MSI and SPOT-7 images: A case study from Anamur (Mersin), Turkey," *IEEE J. Sel. Topics Appl. Earth Observ. Remote Sens.*, vol. 13, pp. 2769–2777, May 2020, doi: 10.1109/JSTARS.2020.2996315.

[33] M. A. Aguilar, R. Jiménez-Lao, and F. J. Aguilar, "Evaluation of object-based greenhouse mapping using WorldView-3 VNIR and SWIR data: A case study from Almería (Spain)," *Remote Sens.*, vol. 13, no. 11, May 2021, Art. no. 2133, doi: 10.3390/rs13112133.

[34] S. Acharki and B. K. Veettil, "Mapping plastic-covered greenhouse farming areas using high-resolution PlanetScope and RapidEye imagery: Studies from Loukkos perimeter (Morocco) and Dalat City (Vietnam)," *Environ. Sci. Pollut. Res.*, vol. 30, pp. 23012–23022, 2023, doi: 10.1007/s11356-022-23808-w.

[35] Q. Feng et al., "Mapping of plastic greenhouses and mulching films from very high resolution remote sensing imagery based on a dilated and non-local convolutional neural network," *Int. J. Appl. Earth Observ. Geoinf.*, vol. 102, Oct. 2021, Art. no. 102441, doi: 10.1016/j.jag.2021.102441.

[36] B. Jakab, B. van Leeuwen, and Z. Tobak, "Detection of plastic greenhouses using high resolution RGB remote sensing data and convolutional neural network," *J. Environ. Geography*, vol. 14, no. 1/2, pp. 28–46, May 2021, doi: 10.2478/jengeo-2021-0004.

[37] A. Ma, D. Chen, Y. Zhong, Z. Zheng, and L. Zhang, "National-scale greenhouse mapping for high spatial resolution remote sensing imagery using a dense object dual-task deep learning framework: A case study

of China," *ISPRS J. Photogramm. Remote Sens.*, vol. 181, pp. 279–294, Nov. 2021, doi: 10.1016/j.isprsjprs.2021.08.024.

[38] Z. Chen et al., "A convolutional neural network for large-scale greenhouse extraction from satellite images considering spatial features," *Remote Sens.*, vol. 14, no. 19, Sep. 2022, Art. no. 4908, doi: 10.3390/rs14194908.

[39] R. Hong, B. Xiao, H. Yan, J. Liu, P. Liu, and Z. Song, "Multitemporal greenhouse mapping for high-resolution remote sensing imagery based on an improved YOLOX," *Comput. Electron. Agriculture*, vol. 206, Mar. 2023, Art. no. 107689, doi: 10.1016/j.compag.2023.107689.

[40] C. Deng and C. Wu, "BCI: A biophysical composition index for remote sensing of urban environments," *Remote Sens. Environ.*, vol. 127, pp. 247–259, Dec. 2012, doi: 10.1016/j.rse.2012.09.009.

[41] P. Zhang et al., "A novel index for robust and large-scale mapping of plastic greenhouse from Sentinel-2 images," *Remote Sens. Environ.*, vol. 276, Jul. 2022, Art. no. 113042, doi: 10.1016/j.rse.2022.113042.

[42] M. A. Aguilar, R. Jiménez-Lao, C. Ladisa, F. J. Aguilar, and E. Tarantino, "Comparison of spectral indices extracted from Sentinel-2 images to map plastic covered greenhouses through an object-based approach," *GISci. Remote Sens.*, vol. 59, no. 1, pp. 822–842, May 2022, doi: 10.1080/15481603.2022.2071057.

[43] G. X. Zhao, J. Li, T. Li, Y. D. Yue, and T. Warner, "Utilizing Landsat TM imagery to map greenhouses in Qingzhou, Shandong Province, China," *Pedosphere*, vol. 14, no. 3, pp. 363–369, 2004.

[44] E. A. L. Salas and G. M. Henebry, "Separability of maize and soybean in the spectral regions of chlorophyll and carotenoids using the Moment Distance Index," *Isr. J. Plant Sci.*, vol. 60, no. 1/2, pp. 65–76, 2012, doi: 10.1560/ijps.60.1-2.65.

[45] L. Ji et al., "Object-based mapping of plastic greenhouses with scattered distribution in complex land cover using Landsat 8 OLI images: A case study in Xuzhou, China," *J. Indian Soc. Remote Sens.*, vol. 48, no. 2, pp. 287–303, 2020, doi: 10.1007/s12524-019-01081-8.

[46] P. Zhang et al., "Pixel–scene–pixel–object sample transferring: A labor-free approach for high-resolution plastic greenhouse mapping," *IEEE Trans. Geosci. Remote Sens.*, vol. 61, Mar. 2023, Art. no. 4401717, doi: 10.1109/TGRS.2023.3257293.

[47] X. Zhang, B. Cheng, J. Chen, and C. Liang, "High-resolution boundary refined convolutional neural network for automatic agricultural greenhouses extraction from GaoFen-2 Satellite imageries," *Remote Sens.*, vol. 13, no. 21, Oct. 2021, Art. no. 4237, doi: 10.3390/rs13214237.

[48] European Space Agency, "Sentinel-2 user handbook," Jul. 2015. [Online]. Available: https://sentinels.copernicus.eu/documents/247904/685211/Sentinel-2_User_Handbook

[49] D. Scheffler, A. Hollstein, H. Diedrich, K. Segl, and P. Hostert, "AROSICS: An automated and robust open-source image co-registration software for multi-sensor satellite data," *Remote Sens.*, vol. 9, no. 7, Jul. 2017, Art. no. 676, doi: 10.3390/rs9070676.

[50] S. K. McFeeters, "The use of the normalized difference water index (NDWI) in the delineation of open water features," *Int. J. Remote Sens.*, vol. 17, no. 7, pp. 1425–1432, Jan. 1996, doi: 10.1080/01431169608948714.

[51] H. Xu, "Modification of normalised difference water index (NDWI) to enhance open water features in remotely sensed imagery," *Int. J. Remote Sens.*, vol. 27, no. 14, pp. 3025–3033, Jan. 2006, doi: 10.1080/01431160600589179.

[52] T. Acharya, D. Lee, I. Yang, and J. Lee, "Identification of water bodies in a Landsat 8 OLI image using a J48 decision tree," *Sensors*, vol. 16, no. 7, Jul. 2016, Art. no. 1075, doi: 10.3390/s16071075.

[53] X. Liu et al., "High-resolution multi-temporal mapping of global urban land using Landsat images based on the Google Earth Engine Platform," *Remote Sens. Environ.*, vol. 209, pp. 227–239, May 2018, doi: 10.1016/j.rse.2018.02.055.

Manuel A. Aguilar received the Ph.D. degree in agricultural engineering from the University of Córdoba, Córdoba, Spain, in 2001.

After two years in a Spanish engineering company, he has been, since 1999, with the Department of Engineering, Almera University, Almería, Spain, where he is currently a Full Professor. His research interests include very high resolution commercial satellite imagery, specifically sensor orientations for single and stereo images, orthorectification, classification of land cover, as well as the generation and quality control of digital surface modes. His current research project is focused on mapping greenhouses and identification of protected horticultural crops through object-based image analysis and satellite imagery time series.

Fernando J. Aguilar received the Ph.D. degree in agricultural engineering from the University of Córdoba, Córdoba, Spain, in 1997.

He is currently a Full Professor with the Department of Engineering, University of Almería, Almería, Spain. He is leading and collaborating in research projects related to geospatial data fusion, natural resource monitoring, and mapping from VHR satellite data. He is the coauthor of several international publications. His research interests include digital elevation modeling, airborne and terrestrial laser scanning, digital photogrammetry, and GIS.

Dr. Aguilar is a Reviewer for many of the leading GIS and remote sensing journals around the world. In addition, he has participated as a Guest Editor in JCR indexed journals. He is also a Member of the editorial board of international journals such as Sensors *(Remote Sensors, Control and Telemetry Section)* and Remote Sensing *(Remote Sensor Image Processing Section)*.

Abderrahim Nemmaoui received the Graduate degree in sciences and techniques for the environment protection from the University Cadi Ayyad-Beni Mellal, Marrakech, Morocco, in 2002, the Ph.D. degree in doctoral program groundwater and the environment from the University of Almeria (UAL), Almería, Spain, in November 2011, and the Ph.D. degree in doctoral program greenhouse technology and industrial and environmental engineering from UAL in April 2020.

His research interests include environment, remote sensing, and vegetation mapping.

Gizem Senel received the B.Sc., M.Sc., and Ph.D. degrees in geomatics engineering from Istanbul Technical University, Istanbul, Turkey, in 2017, 2019, and 2023, respectively.

Her Ph.D. education is supported with the scholarship by The Scientific and Technological Research Council, Turkey, and the Council of Higher Education, Turkey. She completed a part of her Ph.D. research at Almeria University, Almería, Spain, as a Ph.D. Scholar of The Scientific and Technological Research Council. Her research focuses on remote sensing applications, including supervised or unsupervised classification methods on mapping plastic-covered greenhouses, determination of water bodies and coastlines, vegetation, and forests, and time-series data analysis.

Cigdem Goksel received the B.Sc., M.Sc., and Ph.D. degrees from the Department of Geomatics Engineering, Istanbul Technical University (ITU), Istanbul, Turkey, in 1984, 1988, and 1996, respectively.

She was a Visiting Scholar with the Mid-America Remote Sensing Center, Murray State University, Murray, KY, USA, in 1999. She is currently a Full Professor with the Department of Geomatic Engineering, ITU. She was involved in several research studies and projects in the field of remote sensing and integrated technologies. She has authored or coauthored more than 130 scientific publications in the remote sensing domain such as urbanization detection, coastal line monitoring, and agricultural and epidemologic studies. Her research interests include monitoring land use/land cover change, remote sensing, and GIS integration for the environmental studies.